PNAS RESEARCH ARTICLE | CHEMISTRY

Ferromagnetic ordering correlated strong metal–oxygen hybridization for superior oxygen reduction reaction activity

Jisi Li[a,1], Caiyan Zheng[b,1], Erling Zhao[a], Jing Mao[a], Yahui Cheng[c], Hui Liu[a,2], Zhenpeng Hu[b,2], and Tao Ling[a,2]

Edited by Alexis Bell, University of California, Berkeley, CA; received May 11, 2023; accepted September 6, 2023

The efficiency of transition-metal oxide materials toward oxygen-related electrochemical reactions is classically controlled by metal–oxygen hybridization. Recently, the unique magnetic exchange interactions in transition-metal oxides are proposed to facilitate charge transfer and reduce activation barrier in electrochemical reactions. Such spin/magnetism-related effects offer a new and rich playground to engineer oxide electrocatalysts, but their connection with the classical metal–oxygen hybridization theory remains an open question. Here, using the $Mn_xV_yO_z$ family as a platform, we show that ferromagnetic (FM) ordering is intrinsically correlated with the strong manganese (Mn)–oxygen (O) hybridization of Mn oxides, thus significantly increasing the oxygen reduction reaction (ORR) activity. We demonstrate that this enhanced Mn–O hybridization in FM Mn oxides is closely associated with the generation of active Mn sites on the oxide surface and obtaining favorable reaction thermodynamics under operating conditions. As a result, FM-$Mn_2V_2O_7$ with a high degree of Mn–O hybridization achieves a record high ORR activity. Our work highlights the potential applications of magnetic oxide materials with strong metal–oxygen hybridization in energy devices.

electrocatalysis | magnetic ordering | metal–oxygen hybridization

Transition-metal oxides (1) have received intensive attention from both academia and industry because of their great potential as electrocatalysts for oxygen-related reactions (2) in economically alkaline polymer electrolyte fuel cells (3) and alkaline electrolysers (4). In the past decades, numerous investigations have been devoted to improving the performance of oxide electrocatalysts (5, 6) through nanostructuring (7, 8), defect introducing (9, 10), doping (11, 12), and/or phase transition (13, 14). Despite great progresses, current performance of oxide electrocatalysts has entered the bottleneck stage, and little room is left for further improvement through material/structure engineering.

Magnetic and spin effects hold promise for advancing oxygen electrocatalysis (15–26). It has been experimentally proved that the introduction of magnetic field can improve the catalytic efficiency by promoting gas/liquid diffusion (27). Besides, it has recently been revealed that the intrinsic activity of electrocatalysts is closely related to their internal spin polarization and spin/magnetic interactions (15, 28). Specifically, an electrocatalyst with sufficient spin polarization is able to donate/accept electrons with appropriate electrons' spin (e-spin) from/to the reaction intermediates to balance the spin of oxygen molecules with a ground triplet state, and thus accelerating oxygen electrocatalysis by allowing spin conservation throughout the reaction (15, 16, 19, 20, 29, 30). For example, chiral molecules and biologically active centers ingeniously build spin-selective channels to exact e-spins with the "correct" orientation, resulting in ultrahigh reaction turnover frequencies (16, 17). Therefore, transition-metal oxides with intrinsic magnetic ordering are highly expected to achieve spin selectivity through unique magnetic exchange interactions (18–20).

On the other hand, during the past decades, intensive research efforts have been paid to explore electronic structure descriptors [e_g filling (31, 32), p-band centre (33, 34), metal–oxygen hybridization (35–37), etc.] to provide a guideline for the design of highly active oxide materials. In particular, metal–oxygen hybridization (1, 38), which can well describe the charge transfer between active metal sites and oxygen intermediates, has been proved to govern the activity of oxide electrocatalysts. In view of recent advances in spin-enhanced oxygen electrocatalysis, revealing possible correlation among magnetic ordering, metal–oxygen hybridization, and resulting changes in electrochemical property of magnetic oxides will undoubtedly deepen the understanding of oxygen-related reactions; however, this remains largely unexplored.

Herein, using $Mn_xV_yO_z$ family as a platform, we probe the intrinsic correlation among magnetic ordering, metal–oxygen hybridization, and oxygen reduction reaction (ORR) activity. We quantify the same Mn oxides with ferromagnetic (FM) and antiferromagnetic (AFM) orderings and show that FM ordering greatly enhances the manganese

Significance

Transition-metal oxides are cost-effective and earth-abundant electrocatalysts for economically alkaline polymer electrolyte fuel cells and alkaline electrolysers. For transition-metal oxides, they usually exhibit different magnetic states, namely ferromagnetic (FM) ordered state, antiferromagnetic (AFM) ordered state, paramagnetic state, etc. The intrinsic connection between the magnetic state and performance of transition-metal oxides remains an open question. In this work, we show that FM ordering of transition-metal oxides is closely related with their metal–oxygen hybridization, a property that is considered to govern the performance of transition-metal oxides. Our work bridges the gap between the classic metal–oxygen hybridization theory and understanding of oxides from spin/magnetism perspective and helps transition magnetic oxides to break through their activity limits.

Author contributions: T.L. designed research; J.L., C.Z., E.Z., and J.M. performed research; Y.C. contributed new reagents/analytic tools; H.L., Z.H., and T.L. analyzed data; and T.L. wrote the paper.

The authors declare no competing interest.

This article is a PNAS Direct Submission.

[1]J.L. and C.Z. contributed equally to this work.

[2]To whom correspondence may be addressed. Email: hui_liu@tju.edu.cn, zphu@nankai.edu.cn, or lingt04@tju.edu.cn.

This article contains supporting information online at https://www.pnas.org/lookup/suppl/doi:10.1073/pnas.2307901120/-/DCSupplemental.

Published October 16, 2023.

(Mn)–oxygen (O) hybridization, which accelerates the electron transfer between surface Mn sites and adsorbed oxygen species in the electrolyte, thereby facilitating the evolution of surface Mn ions to active Mn^{3+} species during the reaction, evidenced by quantitative cyclic voltammetry (CV), in situ X-ray absorption near edge structure (XANES), and in situ ultraviolet–visible (UV–Vis) spectroscopy. Moreover, we reveal that the enhanced Mn–O hybridization enables Mn oxide with FM ordering to achieve a favorable reaction path under working conditions, demonstrated by density functional theory (DFT) calculations. As a consequence, $Mn_2V_2O_7$ with FM ordering affords a superior high ORR activity, outperforming the state-of-the-art Pt/C catalyst. More importantly, $Mn_2V_2O_7$ exhibits a positive magnetic response under an external magnetic field.

Results

Magnetic Orderings of $Mn_2V_2O_7$ and MnV_2O_6. Manganese-based oxides are one of the most active materials towards ORR (39). In this work, we investigated the $Mn_xV_yO_z$ family, in which edge-sharing magnetic [MnO_6] octahedron layers with identical Mn^{2+} magnetic moment of 4.58 μ_B are separated by the nonmagnetic [VO_n] layers. $Mn_2V_2O_7$ and MnV_2O_6 are two typical oxides in $Mn_xV_yO_z$ family with $C2/m$ space group (Fig. 1 *A* and *C*), exhibiting FM and AFM orderings, respectively. That is, the e-spins of adjacent Mn ions in each [MnO_6] layer of $Mn_2V_2O_7$ and MnV_2O_6 are in the same and opposite directions, respectively (Fig. 1 *B* and *D*).

We experimentally investigated the magnetic properties of $Mn_2V_2O_7$ and MnV_2O_6 using vibrating sample magnetometer. Note that these two oxides were fabricated by cation exchange method (40) using the same sacrificial template to make sure that they possess similar morphology and surface area (Fig. 1*E* and *SI Appendix*, Figs. S1–S4). As-fabricated $Mn_2V_2O_7$ shows an alternating Mn and V atomic layer structure (Fig. 1 *F*, *Inset*). Moreover, as illustrated in Fig.1*F*, $Mn_2V_2O_7$ exhibits obvious hysteresis in the range of ±10,000 Oe with a saturation magnetization of ~18.3 emu g^{-1}, confirming its long-range FM ordering of $Mn_2V_2O_7$, while MnV_2O_6 shows a typical AFM behaviour with a tiny magnetic susceptibility (~4.4 × 10^{-5} emu g^{-1} Oe^{-1}).

Correlation between Magnetic Ordering and Mn–O Hybridization. To better understand the relationship between magnetic ordering and Mn–O hybridization, we calculated the electronic states of Mn-3*d* and O-2*p* of $Mn_2V_2O_7$ and MnV_2O_6 with both FM and AFM orderings (*SI Appendix*, Fig. S5). As shown in Fig. 2*A*, the projected Mn-3*d* orbitals of FM-$Mn_2V_2O_7$ are highly spin-polarized, where all the occupied states are in the same spin channel. More importantly, a strong hybridization between the Mn-3*d* and O-2*p* orbitals is observed near the Fermi level. In contrast, for AFM-$Mn_2V_2O_7$, the Mn-3*d* states in valence and conduction bands are symmetrically distributed. A similar case is also observed in MnV_2O_6 with FM and AFM orderings (Fig. 2*B*).

Moreover, we quantified the hybridization degree of Mn-3*d* and O-2*p* orbitals in $Mn_2V_2O_7$ and MnV_2O_6 by analysing their projected density of states (PDOS, *SI Appendix*, Figs. S6 and S7). Since highly spin-polarized states are observed in manganese oxides with FM ordering–the electronic states near the Fermi level are mainly contributed by Mn-3*d* and O-2*p* in spin-up channel; here, we only considered the electronic states in the spin-up channel to quantify metal–oxygen hybridization (41, 42). Specifically, the hybridization degree between Mn-3*d* and O-2*p* orbital is defined as: $\frac{DOS_{overlapped}}{DOS_{O-2p\ states}}$ (38, 43), where $DOS_{overlapped}$ and $DOS_{O-2p\ states}$ are the integration of the overlapping O-2*p* with Mn-3*d* states and the total O-2*p* states, respectively, in the spin-up channel from –6 to 0 eV. Note that both FM and AFM ordering

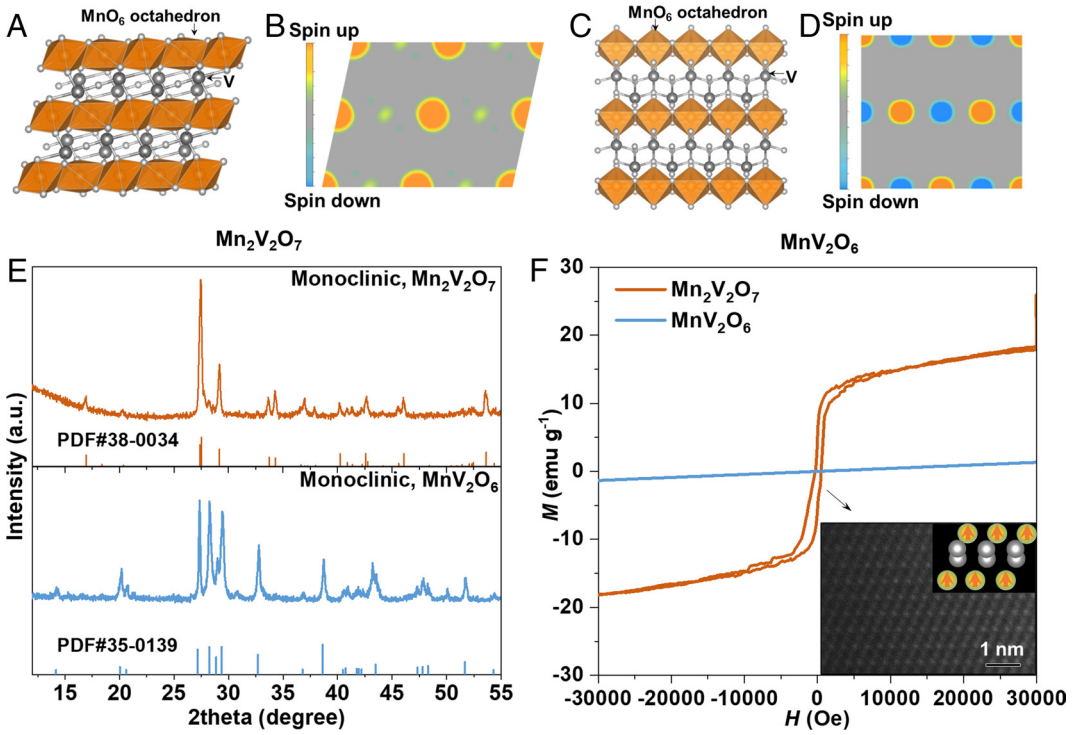

Fig. 1. Magnetic structure of $Mn_2V_2O_7$ and MnV_2O_6. (*A*) Crystal structure of $Mn_2V_2O_7$. (*B*) Spin distribution map of $Mn_2V_2O_7$ (010) plane. (*C*) Crystal structure of MnV_2O_6. (*D*) Spin distribution map of MnV_2O_6 (100) plane. (*E*) XRD patterns of $Mn_2V_2O_7$ and MnV_2O_6. (*F*) Magnetic hysteresis loops of $Mn_2V_2O_7$ and MnV_2O_6, with the *Inset* showing the atomic-scale high-angle annular dark-field scanning transition electron microscopic image of $Mn_2V_2O_7$.

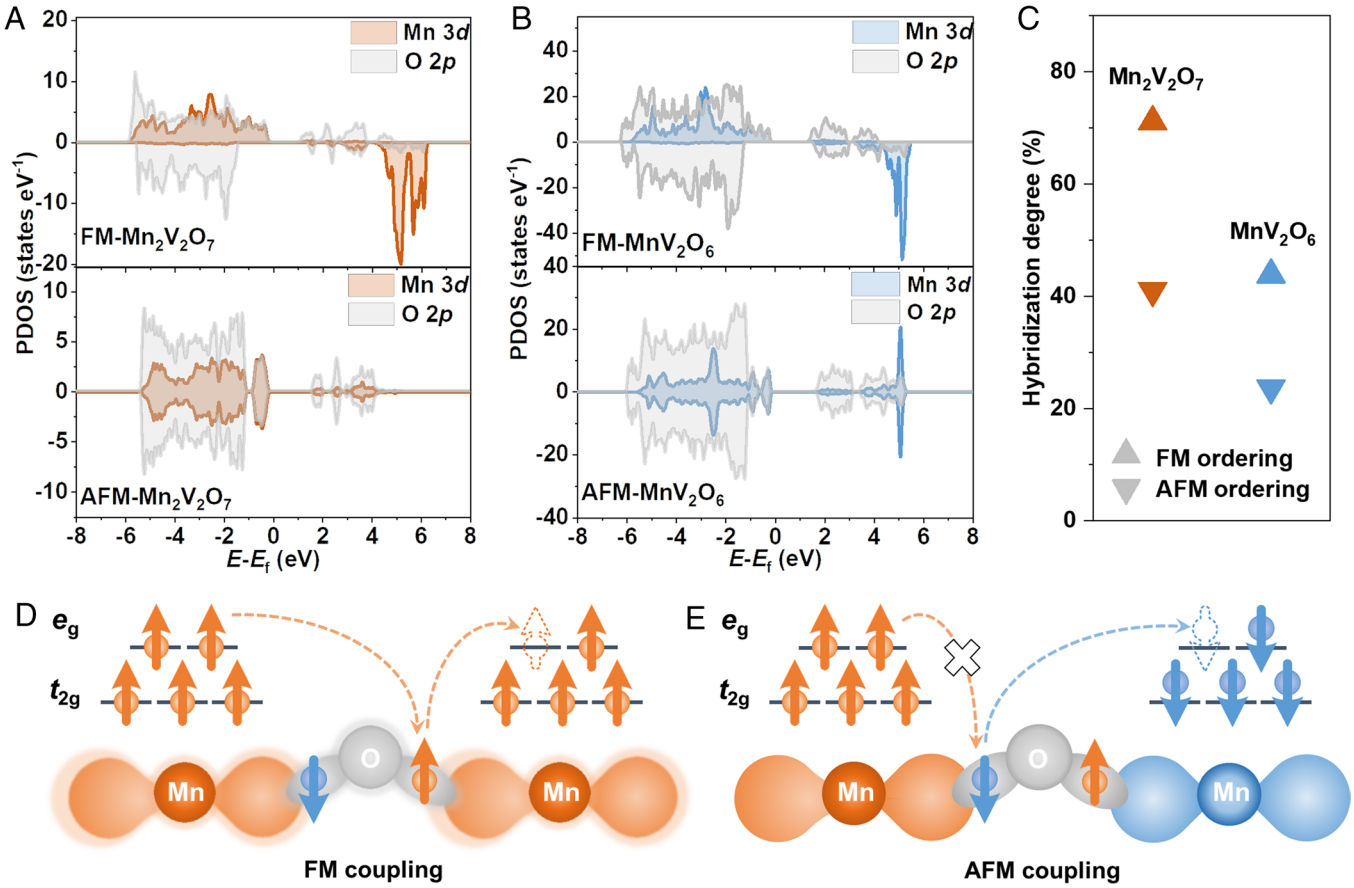

Fig. 2. Correlation between magnetic ordering and metal–oxygen hybridization. (*A* and *B*) PDOS of $Mn_2V_2O_7$ and MnV_2O_6 with FM and AFM orderings, respectively. (*C*) Hybridization degrees of $Mn_2V_2O_7$ and MnV_2O_6 with FM and AFM orderings. (*D* and *E*) Schematic diagrams of FM and AFM interactions, respectively.

were considered for the same oxide to focus on the effect of magnetic ordering on metal–oxygen hybridization and to exclude the influence of other structural factors (1, 32), such as metal valence state, crystal structure, etc. Impressively, the hybridization degree of Mn-3*d* and O-2*p* orbitals in $Mn_2V_2O_7$ increases from ~41% for AFM to ~71% for FM ordering (Fig. 2*C*). A similar enhancement of Mn–O orbital hybridization is also found in MnV_2O_6 from AFM to FM ordering (Fig. 2*C*). These collective results reveal a clear correlation between magnetic ordering (FM/AFM) and Mn–O hybridization, which can explain that FM exchange interaction in Mn oxides promotes delocalization of parallel spins in the Mn–O bonds and facilitates easy electron transition between interconnected Mn and O ions (*SI Appendix*, Figs. S6 and S7 and Table S1), thus enhancing Mn–O hybridization, and vice versa (19, 22, 38, 44, 45) (Fig. 2*D*). In contrast, AFM exchange interaction in Mn oxides inhibits electron transition between interconnected Mn and O ions, thereby reducing Mn–O hybridization, and vice versa (Fig. 2*E*).

Monitoring In Situ Evolution of Mn Sites. It has been recently revealed that the metal sites in most transition-metal oxides undergo dynamical changes, and the newly formed metal sites induced by the applied voltage and electrolyte serve as the "real" active sites in electrochemical reactions (46, 47). It is expected that the strong metal–oxygen hybridization in FM oxides will enable the metal sites to rapidly donate/accept electrons from/to adsorbed oxygen species in the electrolyte, thereby facilitating the formation of active metal sites in electrochemical reactions (31, 36, 48, 49). Here, we monitored the dynamic changes of Mn sites in fabricated $Mn_2V_2O_7$ and MnV_2O_6 by CV in argon-saturated 1.0 M KOH at potentials from 0 to 1.20 V versus reversible hydrogen electrode (RHE). It is worth noticing that the experimentally fabricated $Mn_2V_2O_7$ and MnV_2O_6 afford FM and AFM orderings, respectively, as aforementioned (Fig. 1*F*). As illustrated in Fig. 3*A*, the two oxides show quite different redox characteristics, although they exhibit the same initial Mn valence states of +2. More specifically, the anodic and cathodic peak intensities of FM-$Mn_2V_2O_7$ are much higher than those of AFM-MnV_2O_6, especially the anodic $Mn^{2+}\rightarrow Mn^{3+}$ peak at 0.92 V_{RHE}. This result indicates a greatly enhanced transformation of Mn^{2+} to Mn^{3+} on the surface of FM-$Mn_2V_2O_7$ as the applied anodic potential increases.

Notably, Mn^{3+} sites with e_g electron-filling of ~1 are the active sites of Mn oxides towards ORR (32); however, Mn^{3+} is energetically unstable on the surface of Mn oxides due to the single e_g orbital occupying (50, 51). We quantified the Mn^{3+} site densities on FM-$Mn_2V_2O_7$ and AFM-MnV_2O_6 based on a detailed analysis of the CV curves (*SI Appendix*, *Note S1*, Figs. S8 and S9, and Tables S2 and S3). It is exciting to find that the site density of Mn^{3+} on FM-$Mn_2V_2O_7$ is ~6 times higher than that on AFM-MnV_2O_6 at the ORR onset potential (Fig. 3 *A*, *Inset*). This finding is supported by the in situ Mn *K*-edge XANES that the measured average Mn valence of FM-$Mn_2V_2O_7$ is beyond 3+ at 1.20 V_{RHE} due to the formation of large amounts of Mn^{3+} during the reaction (Fig. 3*B* and *SI Appendix*, Figs. S10 and S11 and Table S4). In contrast, AFM-MnV_2O_6 exhibits a significantly lowered Mn valence state under identical working conditions (*SI Appendix*, Fig. S12 and Table S5). Such substantial increase of

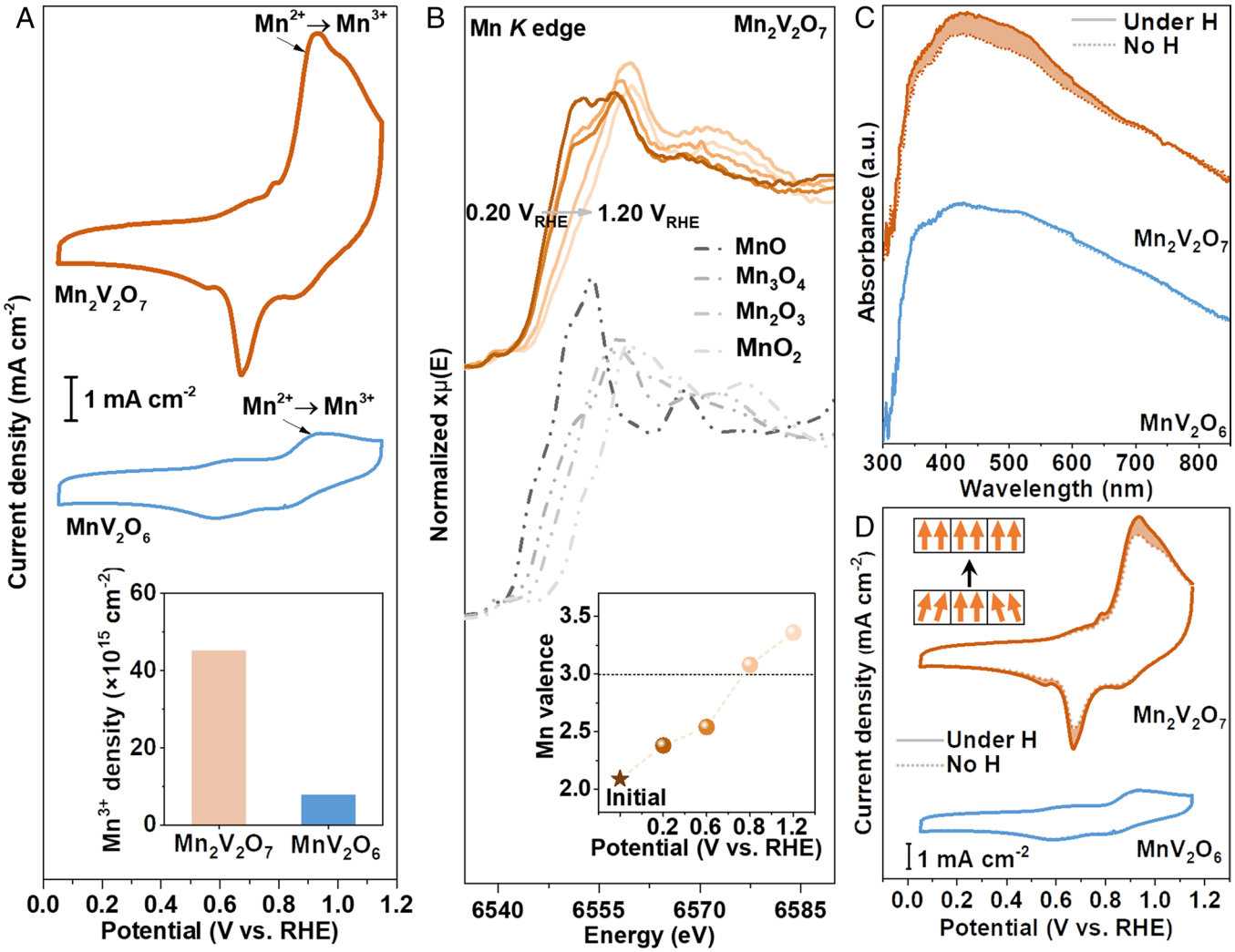

Fig. 3. In situ evolution of Mn sites on $Mn_2V_2O_7$ and MnV_2O_6. (*A*) CV curves of $Mn_2V_2O_7$ and MnV_2O_6 in Ar-saturated 1.0 M KOH at a scan rate of 50 mV s^{-1}, with the *Inset* showing Mn^{3+} site densities of $Mn_2V_2O_7$ and MnV_2O_6 at ~1.20 V_{RHE}. (*B*) In situ XANES spectra of $Mn_2V_2O_7$ at different potentials, with the *Inset* showing the corresponding Mn valences. (*C*) In situ UV–Vis spectra of $Mn_2V_2O_7$ at 0.9 V_{RHE} and MnV_2O_6 at 1.0 V_{RHE} under magnetic field (H) and with no H. (*D*) CV curves of $Mn_2V_2O_7$ and MnV_2O_6 in Ar-saturated 1.0 M KOH at a scan rate of 50 mV s^{-1} under magnetic field (H) and with no H. The *Inset* schematic diagram shows that the spins in each domain of $Mn_2V_2O_7$ tend to align under the external magnetic field.

Mn^{3+} on FM-$Mn_2V_2O_7$ is in line with our expectation that the strong Mn–O hybridization in FM-$Mn_2V_2O_7$ accelerates the electron transfer of surface Mn sites to adsorbed oxygen species through well-mixed Mn-3*d* and O-2*p* orbitals (Mn^{2+}–O^{2-} ↔ $Mn^{(2+\delta)+}$–$O^{(2-\delta)-}$) (36), thereby facilitating the evolution of Mn^{2+} to Mn^{3+} under working conditions (we have excluded the possibility of facilitated evolution of Mn^{2+} to Mn^{3+} on FM-$Mn_2V_2O_7$ by the enhanced electrical conductivity of FM-$Mn_2V_2O_7$ compared with that of AFM-MnV_2O_6, *SI Appendix*, Fig. S13).

To further confirm the critical role of magnetic ordering in generating active Mn sites in the electrochemical reaction, the response of FM-$Mn_2V_2O_7$ and AFM-MnV_2O_6 under a magnetic field was monitored by in situ UV–Vis spectroscopy, which is sensitive to the changes of valence electron in transition-metal-based materials (50). Spectral changes of FM-$Mn_2V_2O_7$ and AFM-MnV_2O_6 were recorded at varying applied potentials. As illustrated in Fig. 3*C* and *SI Appendix*, Fig. S14, the UV–Vis spectra of AFM-MnV_2O_6 remain unchanged under the magnetic field, while the absorption peak of FM-$Mn_2V_2O_7$ increases by 10% under the magnetic field. According to the literature (50, 52), the peaks of Mn oxides at 350~390 nm and 470~510 nm are assigned to the charge-transfer transition of O^{2-} → Mn^{3+} and the *d*–*d* transition of Mn^{3+}, respectively. The enhanced absorption peaks of FM-$Mn_2V_2O_7$ under the magnetic field indicate that the implementation of field increases the amounts of Mn^{3+} on the surface of FM-$Mn_2V_2O_7$. This finding is further confirmed by the CV analysis that the peak current density of FM-$Mn_2V_2O_7$ increases by 18% under the magnetic field (Fig. 3*D*). Correspondingly, the Mn^{3+} site density on FM-$Mn_2V_2O_7$ is increased by 11% under the magnetic field (*SI Appendix*, Fig. S15 and Table S2). These results are reasonable that the applied magnetic field can align the spins of the individual magnetic domains within a single FM electrocatalyst (Fig. 3 *D*, *Inset*) and promotes the FM exchange interactions (15, 20), thereby enhancing electron delocalization and the evolution of magnetic metal centres.

Magnetic Ordering Adjusted Reaction Thermodynamics. The above results reveal that FM and AFM orderings with different hybridization degrees of Mn–O orbitals have different affinity for oxygen species (53), which will undoubtedly affect the adsorption of oxygen intermediates. To further investigate the magnetic effect on reaction thermodynamics, we constructed $Mn_2V_2O_7$ with FM and AFM orderings (*SI Appendix*, *Note S2* and Tables S6 and S7) and rationally exposed Mn^{3+} sites on the surface of $Mn_2V_2O_7$ (*Inset*

of Fig. 4 *A* and *SI Appendix*, *Note S3*, Figs. S16–S18, and Table S8). We calculated ORR free-energy diagrams on the Mn sites of FM- and AFM-$Mn_2V_2O_7$ (we experimentally exclude V ions as the ORR active sites on $Mn_2V_2O_7$, *SI Appendix*, Fig. S19). As illustrated in Fig. 4*A* and *SI Appendix*, Table S9, the potential-limiting step of AFM-$Mn_2V_2O_7$ is the first reaction step to convert the adsorbed O_2 to *OOH, while the oxygen intermediates bind more strongly on FM-$Mn_2V_2O_7$ to promote the formation of *OOH, and the potential-limiting step transfers to *OH desorption.

Note that the conversion of triplet O_2 to the *OOH intermediate ($O_2 \rightarrow$ *OOH) is generally considered as the main limitation of ORR on oxide materials (59, 60). A stronger Mn–O hybridization with FM ordering is expected to stabilize *OOH, thus increasing the driving force for $O_2 \rightarrow$ *OOH (32). As shown in Fig. 4*B*, FM-$Mn_2V_2O_7$ shows a ~30% increase in Mn–O hybridization compared with AFM-$Mn_2V_2O_7$; correspondingly, the energy consumption of $O_2 \rightarrow$ *OOH on FM-$Mn_2V_2O_7$ is reduced by ~0.1 eV compared with that on AFM-$Mn_2V_2O_7$. This finding demonstrates that the strong Mn–O hybridization by FM ordering promotes the formation of *OOH and greatly enhances the intrinsic activity of each Mn active site on FM-$Mn_2V_2O_7$.

Moreover, we correlated the calculated overpotentials of $Mn_2V_2O_7$ and other reported electrocatalysts with their adsorption-free energies of *OOH intermediate (ΔG_{*OOH}). As shown in Fig. 4*C*, a typical volcano plot was delivered, where FM-$Mn_2V_2O_7$ lies at the volcano peak. Our calculation results highlight the key role of FM ordering with strong Mn–O hybridization in optimizing reaction thermodynamics of magnetic transition-metal oxides.

Magnetic Effect on ORR Activity. We then proceeded to measure the ORR performance of the experimentally fabricated FM-$Mn_2V_2O_7$ and AFM-MnV_2O_6 using a rotating disk electrode in O_2-saturated 1.0 M KOH (*SI Appendix*, Fig. S20). The state-of-the-art Pt/C was included for reference purposes (*SI Appendix*, Fig. S21). As expected, FM-$Mn_2V_2O_7$ shows far better ORR activity than AFM-MnV_2O_6 (Fig. 5*A* and *SI Appendix*, Fig. S22), which should be ascribed to the more Mn^{3+} active sites (Fig. 3 *A* and *B*) and more favorable reaction thermodynamics (Fig. 4) on the former. More impressively, FM-$Mn_2V_2O_7$ exhibits a half-wave potential of 0.89 V_{RHE}, which is even 0.01 V better than that of the benchmark Pt/C catalyst. To better evaluate the intrinsic ORR activity of FM-$Mn_2V_2O_7$ and Pt/C electrocatalysts, their specific surface areas were carefully assessed (*SI Appendix*, Fig. S23). As shown in Fig. 5*B*, the normalized activity of FM-$Mn_2V_2O_7$ with respect to its specific surface area is ~74 μA cm^{-2} at 0.90 V_{RHE}, superior to that of the Pt/C catalyst (~57

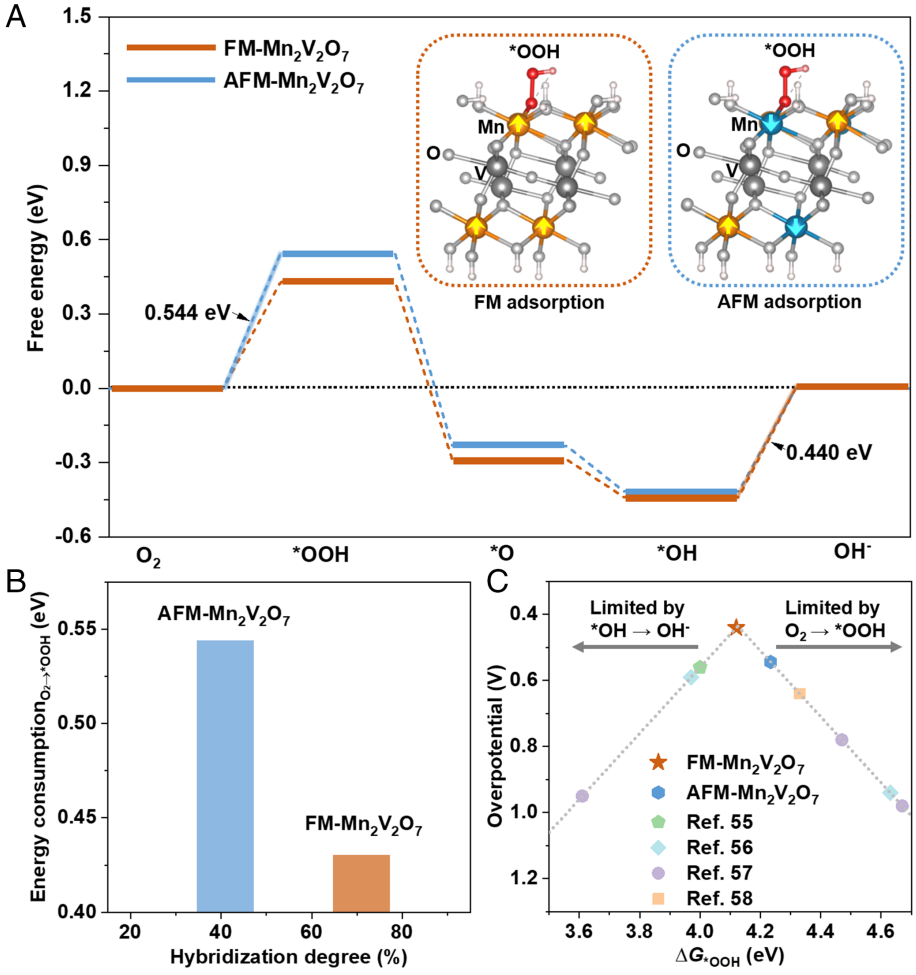

Fig. 4. Magnetic ordering regulated ORR thermodynamics on $Mn_2V_2O_7$. (*A*) ORR free-energy diagrams of $Mn_2V_2O_7$ with FM and AFM orderings at 1.23 V_{RHE}, with the *Inset* showing atomic configurations of *OOH adsorbed on $Mn_2V_2O_7$ (001) surface with FM and AFM orderings. The highlight indicates the potential-limiting step. (*B*) Correlation between energy consumption of $O_2 \rightarrow$ *OOH and hybridization degree. (*C*) Volcano plot of DFT calculated theoretical overpotential as a function of ΔG_{*OOH}. The dashed lines were plotted by the equation (54); η = 1.23 V−{min (4.92 eV−ΔG_{*OOH}, ΔG_{*OH})}/*e*, where $\Delta G_{*OOH} = \Delta G_{*OH}$ + 3.33 eV, and ΔG_{*OH} is the adsorption free energy of *OH intermediate. For comparison, the data points of other transition-metal oxide catalysts are plotted according to the reported works (55–58).

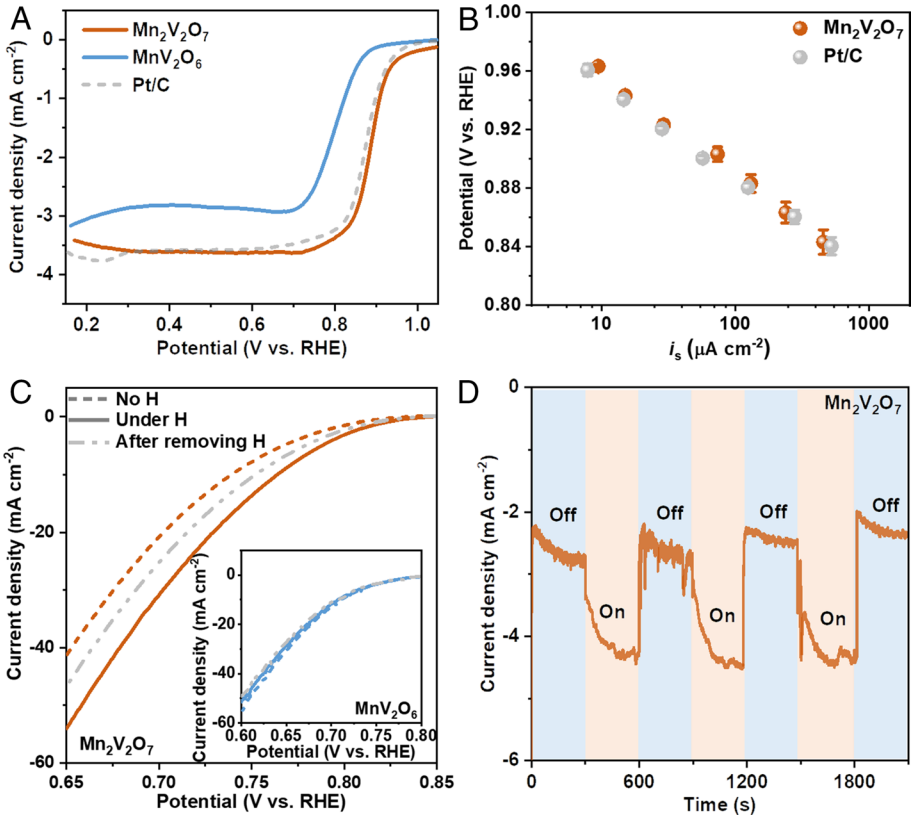

Fig. 5. Magnetic effect on ORR activity. (*A*) ORR polarization curves of $Mn_2V_2O_7$, MnV_2O_6 and Pt/C in O_2-saturated 1.0 M KOH at a scan rate of 5 mV s^{-1} with a rotating rate of 1,600 rpm. (*B*) Specific activities (i_s) of $Mn_2V_2O_7$ and Pt/C. Error bars represent SDs from at least three independent repeated measurements. (*C*) LSV curves of $Mn_2V_2O_7$ and MnV_2O_6 (*Inset*) in O_2-saturated 1.0 M KOH at a scan rate of 5 mV s^{-1} with no magnetic field (H), under magnetic field and after removing magnetic field (~1 T). (*D*) Magneto-chronoamperometry experiment of $Mn_2V_2O_7$ in O_2-saturated 1.0 M KOH at 0.78 V_{RHE}.

μA cm^{-2}) (*SI Appendix*, *Note S4*). Such excellent performance of FM-$Mn_2V_2O_7$ is consistent with the above calculation result that the intrinsic activity of FM-$Mn_2V_2O_7$ locates at the top of the ORR activity volcano plot (Fig. 4*C*). Moreover, we note that FM-$Mn_2V_2O_7$ is among the most active ORR catalysts in alkaline reported so far (*SI Appendix*, Table S10). Besides, the FM-$Mn_2V_2O_7$ catalyst retains its crystal structure without noticeable structural reconstruction during the ORR process (*SI Appendix*, *Note S5* and Fig. S24).

To further confirm the critical role of magnetic ordering in ORR performance, FM-$Mn_2V_2O_7$ and AFM-MnV_2O_6 were loaded onto Teflon-treated carbon fiber paper and their linear sweep voltammetry (LSV) curves were measured under a magnetic field of ~1 T (*SI Appendix*, Fig. S25). As shown in Fig. 5*C*, the current density of FM-$Mn_2V_2O_7$ increases under the external magnetic field, and decreases after the magnetic field was removed (LSV curve does not fully recover to the initial state due to the remanence in FM-$Mn_2V_2O_7$), demonstrating the ORR activity enhancement by the external magnetic field. Moreover, FM-$Mn_2V_2O_7$ shows excellent stability under the magnetic field (*SI Appendix*, Fig. S26). In contrast, AFM-MnV_2O_6 exhibits negligible magnetic response (Fig. 5 *C*, *Inset*), which is consistent with previous reports (15, 30) that the magnetic susceptibility of AFM material is too low, and the applied magnetic field is not strong enough to overcome the AFM coupling.

Notably, we exclude that the activity enhancement of FM-$Mn_2V_2O_7$ originates from magnetohydrodynamic effect (27) on mass transport (e.g., O_2 or solution ion). Specifically, under the same magnetic field conditions, the performance enhancements of AFM-MnV_2O_6 and nonmagnetic Pt/C catalyst are not evident (*Inset* of Fig. 5 *C* and *SI Appendix*, Figs. S27 and S28). Besides, in the absence of magnetic field, the LSV curve of FM-$Mn_2V_2O_7$ remains almost unchanged when the electrolyte was stirred to promote mass transport (*SI Appendix*, Fig. S29). We note that although magnetic field has been reported to enhance mass transport (27), Teflon-treated carbon fiber paper used here can greatly promote O_2 transportation during ORR. Therefore, in our case, the performance enhancement of FM-$Mn_2V_2O_7$ is not caused by magnetic field-promoted mass transport.

Moreover, the response of FM-$Mn_2V_2O_7$ under the magnetic field was further verified by cyclic ON–OFF test. As shown in Fig. 5*D*, the magnetic perturbation was immediate and evident when the magnetic field was applied, and the current density increases by 61%. These results are in good agreement with the above experimentally observations that the external magnetic field can promote the conversion of Mn ions to active Mn^{3+} on FM-$Mn_2V_2O_7$ (Fig. 3 *C* and *D*). Furthermore, it is found that applying a magnetic field increases the reactivity of per active site on FM-$Mn_2V_2O_7$ (*SI Appendix*, Fig. S30), which is consistent with the calculated favorable thermodynamics of FM-$Mn_2V_2O_7$ (Fig. 4).

Discussion

In conclusion, we have found a correlation among magnetic ordering, metal–oxygen hybridization, and electrocatalytic ORR activity of Mn oxides. We show that the optimum transition-metal oxide electrocatalyst should exhibit FM ordering with strong metal–oxygen hybridization, which is conductive to generate large amounts of active sites on the catalyst surface and achieve favourable reaction thermodynamics under working conditions. We

emphasize that for the electrocatalyst near the apex of the activity volcano plot, FM ordering can help the electrocatalyst to break the activity limit to climb to or even beyond the apex of the volcano plot. Our work bridges the gap between the classic theory of metal–oxygen hybridization and the new understanding of magnetic oxides from spin and magnetism perspective, which unambiguously can further advance oxygen electrocatalysis.

Materials and Methods

Synthesis of $Mn_2V_2O_7$ and MnV_2O_6 Catalysts. $Mn_2V_2O_7$ and MnV_2O_6 were synthesized via a facile cation exchange method (40, 55) using ZnO as sacrificial templates. Specifically, ZnO nanosheets were first fabricated on a fluorine-doped tin oxide (FTO) substrate. Then, as-fabricated ZnO nanosheets were exchanged with Mn and V precursors in the gas phase (*SI Appendix*, Fig. S1). In the cation exchange reaction, the FTO-supported ZnO nanosheets were placed in the center of the tube, and the manganese chloride ($MnCl_2$) and the treated vanadium chloride (VCl_3) were placed at 4.5 and 9.5 cm upstream of the tube center, respectively. For $Mn_2V_2O_7$, VCl_3 was deliquesced at 100 °C for 50 min before use, and the furnace was heated to and held at 525 °C for 30 min in 50 s.c.c.m nitrogen gas flow. For MnV_2O_6, VCl_3 was deliquesced at 60 °C for 70 min before use, and the furnace was heated to and held at 495 °C for 30 min in 50 s.c.c.m nitrogen gas flow.

Materials Characterization. X-ray diffraction (XRD) characterization was carried out on a Bruker D8 Advance diffractometer with Cu Kα radiation. Scanning electron microscopy (SEM) was performed on a Hitachi S-4800 SEM. High-angle annular dark-field scanning transition electron microscopy image was collected on a JEOL ARM200F microscope with a STEM aberration corrector operated at 200 kV. The convergent semiangle and collection angle were 21.5 and 200 mrad, respectively. XANES measurements were performed at a Stanford Synchrotron Radiation Light Source. X-ray photoelectron spectroscopy data was recorded using a Kα Thermo fisher spectrometer (Thermo Fisher Scientific). Brunauer–Emmett–Teller surface area was determined from nitrogen adsorption data measured at 77 K on a Microporous instrument Tristar 3000.

Magnetic Property Measurements. Magnetic properties of $Mn_2V_2O_7$ and MnV_2O_6 were measured with a superconducting quantum interference device magnetometer (MPMS XL-7T, Quantum Design). The magnetic hysteresis loop measurements were recorded at room temperature in fields between −30,000 and +30,000 Oe.

In Situ Spectroscopic Characterizations. In situ Mn and V *K*-edge XANES spectra during ORR were recorded using a homemade electrochemical cell with polyimide film windows, and the valence analysis was conducted by the linear combination fitting method. In situ UV–Vis spectra were performed on a Hitachi U-3010 with a homemade photoelectrochemical cell, with catalysts fabricated directly on a FTO substrate as the working electrode, a graphite rod as the counter electrode, and a saturated calomel as the reference electrode.

Electrochemical Characterizations. The electrocatalytic performance of the oxide catalysts was measured on a WaveDriver 20 electrochemical workstation (Pine Research Instrument). The reference electrode was a saturated calomel and the counter electrode was a graphite rod. The catalyst ink was prepared by dispersing 5 mg catalyst, 5 mg carbon powder (Vulcan XC 72), and 50 μL Nafion solution (5 wt%) in 1 mL deionized water. Afterwards, the ink solution was sonicated for 30 min to get a uniform suspension. The well-dispersed catalyst ink was dropped onto a polished glassy-carbon rotating disk electrode (0.196 cm^2) to maintain a catalyst mass-loading of 0.25 mg cm^{-2} for all measurements. A Pt/C (20 wt%) catalyst was used as a reference. Potentials were calibrated to RHE in the high-purity H_2-saturated 1.0 M KOH solution (61) (*SI Appendix*, Fig. S31). The CV curves were recorded at a scan rate of 50 mV s^{-1}. The LSV curves were recorded at a scan rate of 5 mV s^{-1} at 1,600 rpm until the CV signals were stable (at least 20 sweeps).

For LSV curves under a magnetic field, a Hall Effect Test System (CH-100) was used to apply the magnetic field (*SI Appendix*, Fig. S25). The LSV curve was first recorded in the absence of an applied magnetic field (marked as "no H"). Then, an external magnetic field of 1T was applied to magnetize the electrode for 10 min, and the LSV curve was recorded under the field (marked as "under H"). Finally, the magnetic field was removed, and the LSV curve was remeasured (marked as "after removing H").

Computational Methods. The spin-polarized DFT calculations were implemented in Vienna Ab initio Simulation Package (62) using the projector augmented wave (63) pseudopotential and Perdew–Burke–Ernzerhof (64) exchange-correlation functional. In bulk and surface calculations, convergence conditions were set as 0.02 eV $Å^{-1}$ for force on each atom and 10^{-5} eV for energy. A plane wave kinetic energy cut-off of 500 eV was adopted. $Mn_2V_2O_7$ and MnV_2O_6 bulks (*SI Appendix*, Fig. S5) with a monoclinic structure of space group *C*2/*m*, and $Mn_2V_2O_7$ (001) surface (*SI Appendix*, Fig. S16) with a vacuum layer of 15 Å were studied. The Brillouin zone was sampled by the Monkhorst–Pack scheme, namely, a 3×4×2 *k*-point for the MnV_2O_6 bulk, a 5×4×6 *k*-point for the $Mn_2V_2O_7$ bulk, and a 5×5×1 *k*-point for the $Mn_2V_2O_7$ (001). The $Mn_2V_2O_7$ (001) slab (a = 6.54 Å, b = 8.97 Å) contains 50 atoms including 12 H atoms. During surface optimizations, the bottom H–O–Mn layers were fixed while other atomic layers were fully relaxed. FM and AFM structures were constructed by setting the Mn atomic spins. The Hubbard U approach (65) was used to describe strongly correlated *d*-electron systems, and here, an effective Coulomb parameter (U_{eff}) value of 4.0 eV was applied to Mn 3*d* states and U_{eff} = 3.1 eV for V 3*d* states (66). The Gibbs free-energy change (ΔG) was obtained by

$$\Delta G = \Delta E + \Delta ZPE - T\Delta S - eU, \quad [1]$$

where ΔE is the reaction energy calculated by DFT, ΔZPE and ΔS are the changes in zero-point energy and entropy, respectively, which are related to vibrational frequency, T is the temperature at 298.15 K, e is the elementary charge, and U is the electrode potential. The entropies of gas phase molecules were taken from the National Institute of Standards and Technology database (67).

Data, Materials, and Software Availability. All study data are included in the article and/or *SI Appendix*.

ACKNOWLEDGMENTS. T.L. acknowledged funding from the National Natural Science Foundation of China (52071231 and 51722103) and the Natural Science Foundation of Tianjin city (19JCJQJC61900). Z.P. Hu acknowledged funding from the National Natural Science Foundation of China (21933006 and 21773124) and the Fundamental Research Funds for the Central Universities Nankai University (No. 63213042, 63221346, and ZB22000103). Calculations were performed on Supercomputing Center of Nankai University and TianHe-1A at the National Supercomputer Center, Tianjin.

Author affiliations: [a]School of Materials Science and Engineering, Tianjin University, Tianjin 300072, China; [b]School of Physics, Nankai University, Tianjin 300071, China; and [c]Department of Electronics, Nankai University, Tianjin 300350, China

1. J. Hwang *et al.*, Perovskites in catalysis and electrocatalysis. *Science* **358**, 751–756 (2017).
2. Y. Jiao, Y. Zheng, M. Jaroniec, S. Z. Qiao, Design of electrocatalysts for oxygen- and hydrogen-involving energy conversion reactions. *Chem. Soc. Rev.* **44**, 2060–2086 (2015).
3. Y. J. Wang, J. Qiao, R. Baker, J. Zhang, Alkaline polymer electrolyte membranes for fuel cell applications. *Chem. Soc. Rev.* **42**, 5768–5787 (2013).
4. R. Subbaraman *et al.*, Trends in activity for the water electrolyser reactions on 3d M(Ni Co, Fe, Mn) hydr(oxy)oxide catalysts. *Nat. Mater.* **11**, 550–557 (2012).
5. J. Guo *et al.*, Direct seawater electrolysis by adjusting the local reaction environment of a catalyst. *Nat. Energy* **8**, 264–272 (2023).
6. K. Du *et al.*, Interface engineering breaks both stability and activity limits of RuO_2 for sustainable water oxidation. *Nat. Commun.* **13**, 5716 (2022).
7. H. Mistry, A. S. Varela, S. Kuhl, P. Strasser, B. R. Cuenya, Nanostructured electrocatalysts with tunable activity and selectivity. *Nat. Rev. Mater.* **1**, 16009 (2016).
8. F. Cheng *et al.*, Rapid room-temperature synthesis of nanocrystalline spinels as oxygen reduction and evolution electrocatalysts. *Nat. Chem.* **3**, 79–84 (2011).
9. J. Xie *et al.*, Defect-rich MoS_2 ultrathin nanosheets with additional active edge sites for enhanced electrocatalytic hydrogen evolution. *Adv. Mater.* **25**, 5807–5813 (2013).
10. T. Ling *et al.*, Engineering surface atomic structure of single-crystal cobalt (II) oxide nanorods for superior electrocatalysis. *Nat. Commun.* **7**, 12876 (2016).

11. J. W. D. Ng *et al.*, Gold-supported cerium-doped NiO_x catalysts for water oxidation. *Nat. Energy* **1**, 16053 (2016).
12. N. Li *et al.*, Influence of iron doping on tetravalent nickel content in catalytic oxygen evolving films. *Proc. Natl. Acad. Sci. U.S.A.* **114**, 1486–1491 (2017).
13. Y. Yu *et al.*, High phase-purity 1T′-MoS_2- and 1T′-$MoSe_2$-layered crystals. *Nat. Chem.* **10**, 638–643 (2018).
14. M. Bajdich, M. García-Mota, A. Vojvodic, J. K. Nørskov, A. T. Bell, Theoretical investigation of the activity of cobalt oxides for the electrochemical oxidation of water. *J. Am. Chem. Soc.* **135**, 13521–13530 (2013).
15. F. A. Garcés-Pineda, M. Blasco-Ahicart, D. Nieto-Castro, N. López, J. R. Galán-Mascarós, Direct magnetic enhancement of electrocatalytic water oxidation in alkaline media. *Nat. Energy* **4**, 519–525 (2019).
16. W. Mtangi *et al.*, Control of electrons' spin eliminates hydrogen peroxide formation during water splitting. *J. Am. Chem. Soc.* **139**, 2794–2798 (2017).
17. Y. Jiao, R. Sharpe, T. Lim, J. W. H. Niemantsverdriet, J. Gracia, Photosystem II acts as a spin-controlled electron gate during oxygen formation and evolution. *J. Am. Chem. Soc.* **139**, 16604–16608 (2017).
18. Z. Sun *et al.*, Regulating the spin state of Fe(III) enhances the magnetic effect of the molecular catalysis mechanism. *J. Am. Chem. Soc.* **144**, 8204–8213 (2022).
19. X. Ren *et al.*, Spin-polarized oxygen evolution reaction under magnetic field. *Nat. Commun.* **12**, 2608 (2021).
20. T. Wu *et al.*, Spin pinning effect to reconstructed oxyhydroxide layer on ferromagnetic oxides for enhanced water oxidation. *Nat. Commun.* **12**, 3634 (2021).
21. J. Gracia, Spin dependent interactions catalyse the oxygen electrochemistry. *Phys. Chem. Chem. Phys.* **19**, 20451–20456 (2017).
22. J. Gracia, R. Sharpe, J. Munarriz, Principles determining the activity of magnetic oxides for electron transfer reactions. *J. Catal.* **361**, 331–338 (2018).
23. J. Li *et al.*, Spin effect on oxygen electrocatalysis. *Adv. Energy Sustainability Res.* **2**, 2100034 (2021).
24. G. Baryshnikov, B. Minaev, H. Agren, Theory and calculation of the phosphorescence phenomenon. *Chem. Rev.* **117**, 6500–6537 (2017).
25. M. Melander, K. Laasonen, H. Jonsson, Effect of magnetic states on the reactivity of an FCC(111) iron surface. *J. Phys. Chem. C* **118**, 15863–15873 (2014).
26. Z. Li *et al.*, V "Bridged" Co-O to eliminate charge transfer barriers and drive lattice oxygen oxidation during water-splitting. *Adv. Funct. Mater.* **31**, 2008822 (2020).
27. Y. Zhang *et al.*, Recent advances in magnetic field-enhanced electrocatalysis. *ACS Appl. Energy Mater.* **3**, 10303–10316 (2020).
28. C. Hunt *et al.*, Quantification of the effect of an external magnetic field on water oxidation with cobalt oxide anodes. *J. Am. Chem. Soc.* **144**, 733–739 (2022).
29. Y. Sun *et al.*, Spin-related electron transfer and orbital interactions in oxygen electrocatalysis. *Adv. Mater.* **32**, 2003297 (2020).
30. R. R. Chen *et al.*, Antiferromagnetic inverse spinel oxide $LiCoVO_4$ with spin-polarized channels for water oxidation. *Adv. Mater.* **32**, 1907976 (2020).
31. J. Suntivich, K. J. May, H. A. Gasteiger, J. B. Goodenough, Y. Shao-Horn, A perovskite oxide optimized for oxygen evolution catalysis from molecular orbital principles. *Science* **334**, 1383–1385 (2011).
32. J. Suntivich *et al.*, Design principles for oxygen-reduction activity on perovskite oxide catalysts for fuel cells and metal–air batteries. *Nat. Chem.* **3**, 546–550 (2011).
33. A. Grimaud *et al.*, Activating lattice oxygen redox reactions in metal oxides to catalyse oxygen evolution. *Nat. Chem.* **9**, 457–465 (2017).
34. J. Hwang *et al.*, Tuning perovskite oxides by strain: Electronic structure, properties, and functions in (electro)catalysis and ferroelectricity. *Mater. Today* **31**, 100–118 (2019).
35. Z.-F. Huang *et al.*, Chemical and structural origin of lattice oxygen oxidation in Co-Zn oxyhydroxide oxygen evolution electrocatalysts. *Nat. Energy* **4**, 329–338 (2019).
36. J. Suntivich *et al.*, Estimating hybridization of transition metal and oxygen states in perovskites from O *K*-edge X-ray absorption spectroscopy. *J. Phys. Chem. C* **118**, 1856–1863 (2014).
37. W. T. Hong *et al.*, Charge-transfer-energy-dependent oxygen evolution reaction mechanisms for perovskite oxides. *Energy Environ. Sci.* **10**, 2190–2200 (2017).
38. M. N. Grisolia *et al.*, Hybridization-controlled charge transfer and induced magnetism at correlated oxide interfaces. *Nat. Phys.* **12**, 484–492 (2016).
39. Y. Aoki *et al.*, *In situ* activation of a manganese perovskite oxygen reduction catalyst in concentrated alkaline media. *J. Am. Chem. Soc.* **143**, 6505–6515 (2021).
40. T. Ling, M. Jaroniec, S.-Z. Qiao, Recent progress in engineering the atomic and electronic structure of electrocatalysts via cation exchange reactions. *Adv. Mater.* **32**, 2001866 (2020).
41. W. E. Pickett, D. J. Singh, Electronic structure and half-metallic transport in the $La_{1-x}Ca_xMnO_3$ system. *Phys. Rev. B* **53**, 1146–1160 (1996).
42. S. Bhattacharjee, U. V. Waghmare, S.-C. Lee, An improved d-band model of the catalytic activity of magnetic transition metal surfaces. *Sci. Rep.* **6**, 35916 (2016).
43. H. Li *et al.*, Metal–oxygen hybridization determined activity in spinel-based oxygen evolution catalysts: A case study of $ZnFe_{2-x}Cr_xO_4$. *Chem. Mater.* **30**, 6839–6848 (2018).
44. J. B. Goodenough, Theory of the role of covalence in the perovskite-type manganites [La, M(II)] MnO_3. *Phys. Rev.* **100**, 564–573 (1955).
45. J. B. Goodenough, A. L. Loeb, Theory of ionic ordering, crystal distortion, and magnetic exchange due to covalent forces in spinels. *Phys. Rev.* **98**, 391–408 (1955).
46. J. Kang *et al.*, Valence oscillation and dynamic active sites in monolayer NiCo hydroxides for water oxidation. *Nat. Catal.* **4**, 1050–1058 (2021).
47. D. Y. Chung *et al.*, Dynamic stability of active sites in hydr(oxy)oxides for the oxygen evolution reaction. *Nat. Energy* **5**, 222–230 (2020).
48. R. P. Forslund *et al.*, Exceptional electrocatalytic oxygen evolution via tunable charge transfer interactions in $La_{0.5}Sr_{1.5}Ni_{1-x}Fe_xO_{4\pm\delta}$ Ruddlesden-Popper oxides. *Nat. Commun.* **9**, 3150 (2018).
49. M. F. Tesch *et al.*, Evolution of oxygen–metal electron transfer and metal electronic states during manganese oxide catalyzed water oxidation revealed with in situ soft X-ray spectroscopy. *Angew. Chem. Int. Ed. Engl.* **58**, 3426–3432 (2019).
50. K. Jin *et al.*, Mechanistic investigation of water oxidation catalyzed by uniform, assembled MnO nanoparticles. *J. Am. Chem. Soc.* **139**, 2277–2285 (2017).
51. K. Takashima, R. Hashimoto, Nakamura, inhibition of charge disproportionation of MnO_2 electrocatalysts for efficient water oxidation under neutral conditions. *J. Am. Chem. Soc.* **134**, 18153–18156 (2012).
52. T. Takashima, A. Yamaguchi, K. Hashimoto, H. Irie, R. Nakamura, In situ UV-vis absorption spectra of intermediate species for oxygen-evolution reaction on the surface of MnO_2 in neutral and alkaline media. *Electrochemistry* **82**, 325–327 (2014).
53. W. T. Hong *et al.*, Toward the rational design of non-precious transition metal oxides for oxygen electrocatalysis. *Energy Environ. Sci.* **8**, 1404–1427 (2015).
54. H. Xu, D. Cheng, D. Cao, X. C. Zeng, A universal principle for a rational design of single-atom electrocatalysts. *Nat. Catal.* **1**, 339–348 (2018).
55. Y. J. Li *et al.*, Multiscale structural engineering of Ni-doped CoO nanosheets for zinc-air batteries with high power density. *Adv. Mater.* **30**, 1804653 (2018).
56. C. Mu *et al.*, Rational design of spinel cobalt vanadate oxide Co_2VO_4 for superior electrocatalysis. *Adv. Mater.* **32**, 1907168 (2020).
57. Y. Tian *et al.*, Engineering crystallinity and oxygen vacancies of Co(II) oxide nanosheets for high performance and robust rechargeable Zn–air batteries. *Adv. Funct. Mater.* **31**, 2101239 (2021).
58. J. Bian *et al.*, Mg doped perovskite $LaNiO_3$ nanofibers as an efficient bifunctional catalyst for rechargeable zinc-air batteries. *ACS Appl. Energy Mater.* **2**, 923–931 (2019).
59. J. Song *et al.*, A review on fundamentals for designing oxygen evolution electrocatalysts. *Chem. Soc. Rev.* **49**, 2196–2214 (2020).
60. H. Li *et al.*, Analysis of the limitations in the oxygen reduction activity of transition metal oxide surfaces. *Nat. Catal.* **4**, 463–468 (2021).
61. Y. Liang *et al.*, Co_3O_4 nanocrystals on graphene as a synergistic catalyst for oxygen reduction reaction. *Nat. Mater.* **10**, 780–786 (2011).
62. G. Kresse, J. Furthmüller, Efficiency of ab-initio total energy calculations for metals and semiconductors using a plane-wave basis set. *Comput. Mater. Sci.* **6**, 15–50 (1996).
63. P. E. Blöchl, Projector augmented-wave method. *Phys. Rev. B* **50**, 17953–17979 (1994).
64. J. P. Perdew, K. Burke, M. Ernzerhof, Generalized gradient approximation made simple. *Phys. Rev. Lett.* **77**, 3865–3868 (1996).
65. S. L. Dudarev, G. A. Botton, S. Y. Savrasov, C. J. Humphreys, A. P. Sutton, Electron-energy-loss spectra and the structural stability of nickel oxide: An LSDA+U study. *Phys. Rev. B* **57**, 1505–1509 (1998).
66. Q. Yan *et al.*, $Mn_2V_2O_7$: An earth abundant light absorber for solar water splitting. *Adv. Energy Mater.* **5**, 1401840 (2015).
67. R. D. Johnson III, Data from "NIST computational chemistry comparison and benchmark database." https://cccbdb.nist.gov/. Deposited 22 May 2022.